

OKINAWA INSTITUTE OF SCIENCE AND TECHNOLOGY  
GRADUATE UNIVERSITY

Thesis submitted for the degree

Doctor of Philosophy

---

# Massively parallel split-step Fourier techniques for simulating quantum systems on graphics processing units

---

by

**James Schloss**

Supervisor: **Thomas Busch**

October, 2019



# Contents

<b>Contents</b>	<b>ii</b>
<b>Introduction</b>	<b>1</b>
<b>1 Engineering NOON states in for one-dimensional quantum gases</b>	<b>1</b>
1.1 Optimization methods . . . . .	2
1.1.1 Nelder–Mead . . . . .	3
1.1.2 Chopped random basis optimal control . . . . .	6
1.2 Shortcuts to adiabaticity . . . . .	7
1.3 Non-adiabatic generation of NOON states in a Tonks–Girardeau gas . . . .	9
1.3.1 Tonks–Girardeau gas . . . . .	10
1.3.2 NOON states in a TG gas . . . . .	10
1.3.3 Optimal control protocols . . . . .	14
1.3.4 Results with STA protocols . . . . .	17
1.4 Outlook . . . . .	24
<b>Bibliography</b>	<b>25</b>

# Chapter 1

## Engineering NOON states in for one-dimensional quantum gases

Until recently, simulations dynamic control protocols to engineer specific quantum states have been difficult to perform on GPU devices without full control of the software, itself. This meant that researchers wishing to engineer specific quantum states by using GPU simulations would be required to have domain-specific knowledge in both software design and quantum mechanics, neither of which are trivial to understand. This chapter serves as motivation for several methods to be discussed in Chapter ?? to allow for the simulation of quantum control methods on GPU devices, with a particular focus on quantum optimal control [1] and Shortcuts To Adiabaticity (STA) [2]. Both of these control protocols will be used in a physical example for the non-adiabatic generation of superposition states in a one-dimensional Tonks–Girardeau (TG) gas [3]. To start, I will discuss the field of optimization algorithms before moving to STA protocols and a physical system using both in practice.

The work in this chapter has been published in New Journal of Physics [3], and in this publication, I performed all calculations for all the figures generated and focused on optimal control methods. The STA protocol was devised by Jérémie Gillet, and the research was supervised by Albert Benseny and Thomas Busch.

## 1.1 Optimization methods

Optimization algorithms have become essential to many areas of modern computing and focus on either minimizing or maximizing a cost function by modifying several control parameters [4]. The number of control parameters create an  $n$ -dimensional space to traverse, and optimization algorithms are tasked at finding the global minimum or maximum of this domain. For certain domains, it is difficult to find a global optimization strategy and many methods instead get caught in local minima while attempting to find the appropriate solution. Because generalized optimization is such a fundamental problem, there are many known optimal control methods, such as gradient descent [5], the Nelder–Mead or simplex method [6], genetic algorithms [7], and many more. Of these, gradient descent is often considered to be one of the easiest to implement with favorable complexity and convergence guarantees, and because of this, it has become ubiquitous in many areas such as machine learning, which is of particular interest for GPU engineering. Even so, there are limitations to gradient descent, such as its dependence on calculating the gradient of the cost function’s solution domain along with lengthy convergence times for high-precision solutions.

For this work, I am primarily interested in the area of quantum optimal control, which is a method typically used to determine the optimal time-dependent control parameters necessary to transform an initial state to a final, desired state [1]. This means that one will often be maximizing the fidelity between states, defined as  $\mathcal{F} = |\langle \psi | \phi \rangle|^2$ , where  $\psi$  is the engineered quantum state and  $\phi$  is the state one is attempting to replicate. This problem can be re-framed as an attempt to find the maximum of a fidelity *landscape*, where each point in the domain is a calculation of the fidelity, itself. This means that each point in the fidelity landscape necessarily involves solving the Schrödinger equation for chosen control parameters. For this reason, I will be introducing a gradient-less (derivative-free) optimization algorithm, the Nelder–Mead (simplex) method, which is often used as a heuristic approach to this problem and there are several known optimizations for this

method [6, 8, 9]. This method is also the recommended optimization algorithm for the chosen quantum optimal control method of the physical example later discussed in this chapter, Chopped RAndom Basis (CRAB) optimal control. This will be further discussed in Section 1.1.2.

### 1.1.1 Nelder–Mead

The Nelder–Mead method is one of the most commonly implemented gradient-less optimization algorithms to-date and relies heavily on the concept of a simplex, which is a generalization of the three-dimensional tetrahedron to  $n$ -dimensions. For example, a 0-simplex is a point, a 1-simplex is a line, a 2-simplex is a triangle, a 3-simplex is a tetrahedron, and so on. If the Nelder–Mead method is attempting to optimize a cost function with  $n$  control parameters, an  $n + 1$  point simplex will be created, and the points of this simplex will be manipulated until they have converged to a minimum or maximum in the domain. For this section, I will focus on the method introduced in the original work by Nelder and Mead in 1965 while working at the National Vegetable Research Station in Warwick, England [6].

For  $P_i \in i = \{0, \dots, n\}$  simplex points with heights of  $y_i \in i = \{0, \dots, n\}$ , the Nelder–Mead method is tasked at minimizing all points such that  $\sqrt{\sum (y_i - \bar{y})^2 / n} < \eta$ , where  $\bar{y}$  denotes the height of the centroid location of the simplex, and  $\eta$  is some pre-defined convergence threshold value. This convergence criteria assumes that if all points have converged with this method, the final location must be the minimum of the optimization domain; however, as mentioned in the previous section, this method may become trapped in a local minimum. At every step in the Nelder–Mead method, the points with the highest and lowest values are determined and denoted as  $P_h$  and  $P_l$ , respectively. In addition, the centroid location is found as  $\bar{P}$ . This method then performs up to three basic operations on the simplex, itself:

**Reflection** For this operation,  $P_h$  is flipped across  $\bar{P}$ , such that the new location,

$$P^* = (1 + \alpha)\bar{P} - \alpha P_h. \quad (1.1)$$

Here,  $\alpha > 0$  is a constant known as the reflection coefficient. After this operation, the new height is compared to  $y_l$ . If it is lower, the method proceeds to an expansion step. Otherwise, the method checks whether the new height is lower than some other  $y_i \in \{0, \dots, n\}, n \neq \{l, h\}$ , and if it is, the point is kept and the method continues to find the new simplex ordering. If it is found that the reflected point,  $P^*$ , is higher in value than all other points, the method then keeps whichever point corresponds to the lowest height between the reflected and previous highest point and proceeds to the contraction step.

**Expansion** For this operation, an expansion is performed, such that the new location,

$$P^{**} = \gamma P^* + (1 - \gamma)\bar{P}. \quad (1.2)$$

Here,  $\gamma > 1$  is a constant known as the expansion coefficient. If the new height is less than the previously lowest point, the expanded point,  $P^{**}$ , is kept, otherwise the reflected point is kept.

**Contraction** For this operation, a contraction is performed, such that the new location,

$$P^{**} = \beta P_h + (1 - \beta)\bar{P}. \quad (1.3)$$

Here,  $0 < \beta < 1$  is a constant known as the contraction coefficient. If the contracted point,  $P^{**}$ , is lower than the previous highest point, the contracted point is kept, otherwise, the entire simplex is contracted closer to the lowest point with  $P_i = (P_i + P_l)/2$ .

Each step in the Nelder–Mead method begins with a proposed reflection of the least

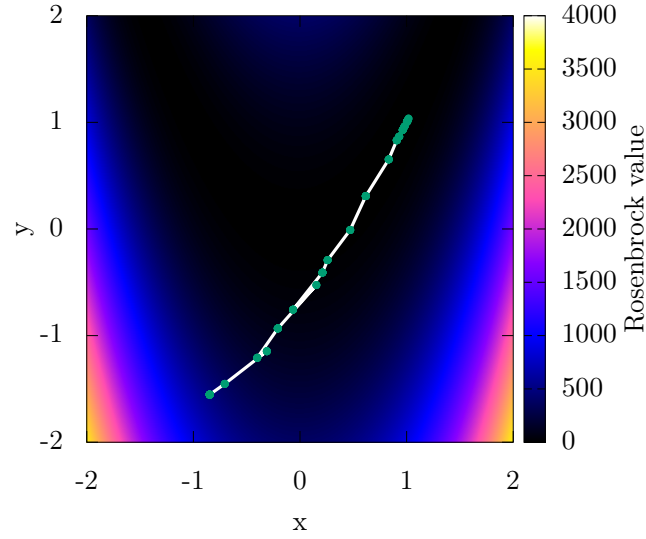


**Figure 1.1:** Plot of the centroid locations (green dots connected with white line) for the Nelder–Mead method while optimizing the Rosenbrock banana function,  $f(x, y) = (a - x)^2 + b(y - x^2)^2$ , with  $a = 1$  and  $b = 100$ . Here, centroid locations start at  $(-0.851, -1.553)$  and end at the known minimum of  $(1, 1)$  in 19 iterations. Here,  $\alpha = 1$ ,  $\beta = 0.5$ , and  $\gamma = 1.5$ .

optimal point about its centroid position. From there, the method follows the protocol described above. The choice of  $\alpha$ ,  $\beta$ , and  $\gamma$  is somewhat arbitrary and should be optimized by-hand. An example of the centroid locations for minimization using this method with the Rosenbrock banana function [10] can be seen in Figure 1.1.

Even though the Nelder–Mead method is a heuristic approach and can become stuck in a local minimum, as long as a sufficient number of random simplexes are chosen at the start of the simulation, it can be used to find an adequately optimal solution. Ultimately, any gradient-less optimization algorithm can be used to traverse the fidelity landscape for quantum optimal control, and in the next section, I will discuss a common method used in the field: the Chopped RAndom Basis (CRAB) optimal control method.

### 1.1.2 Chopped random basis optimal control

The CRAB technique works by modifying a control parameter for a given system,  $\Gamma$ , with a multiplicative term as

$$\Gamma^{\text{CRAB}}(t) = \Gamma^0(t)\gamma(t), \quad (1.4)$$

where  $\Gamma^0(t)$  is an initial guess, and the function  $\gamma(t)$  is written as a sum of  $2J$  sinusoidal functions,

$$\gamma(t) = 1 + \frac{1}{\lambda(t)} \sum_{j=1}^J (A_j \sin(\nu_j t) + B_j \cos(\nu_j t)). \quad (1.5)$$

Here,  $\lambda(t)$  is usually defined by the system, such that  $\Gamma^{\text{CRAB}}$  and  $\Gamma^0$  coincide at initial and final times. This means that  $\lim_{t \rightarrow 0} \lambda(t) = \lim_{t \rightarrow T} \lambda(t) = \infty$ , where  $T$  is the final time of evolution. As such, any smooth function may be chosen with these constraints. For example, one might use

$$\lambda(t) = \frac{T^2}{4t(t-T)}, \quad (1.6)$$

which satisfies the provided conditions. This then transforms the optimal control problem into an optimization of the space spanning  $\{A_j, B_j, \nu_j\}$ , which can be done by using Nelder–Mead with a simplex of random initial points. As an example, if  $J = 10$ , a thirty-dimensional space would be created and a thirty-one simplex would be formed to traverse this space. It is important to remember that each new simplex and simplex-operation requires re-solving the Schrödinger equation for those values, and as such, this is a computational costly technique. Even though higher  $J$  values will produce a more accurate result, lower values should be chosen, if possible.

This method is a general-purpose computational tool for determining the optimal pulse to ensure the generated state is as close to the desired state as possible, and I will show an example of it being used later in this chapter. As such, it is sometimes worthwhile to attempt to devise analytical frameworks that serve a similar purpose, and for certain



systems, this can be done with Shortcuts To Adiabaticity (STA).

## 1.2 Shortcuts to adiabaticity

STA protocols are semi-analytical methods that allow for quantum state generation while retaining the effects of adiabatic movement. Here, adiabatic processes are defined as actions by which slow changes in the control parameters leave particular properties invariant, such as the quantum number [2]. The ultimate goal of STA protocols is to achieve adiabatic motion in sub-adiabatic time, and this can be done in a number of ways; however, in this section, I will introduce only the invariant-based inverse-engineering approach using Lewis–Riesenfeld invariants [11]. In particular, I will focus on the specific methods necessary for the example to be introduced later in this chapter and much of this section will follow traditional derivations from various sources [2, 3, 11].

With the method of Lewis-Riesenfeld invariants, the theory for relating different eigenstates of a time-dependent, Hermitian invariant to the solutions to the Schrödinger equation [12] can be applied to systems with time-dependent Hamiltonians, such that

$$i\hbar \frac{\partial I(t)}{\partial t} - [\hat{\mathcal{H}}, I(t)] = 0, \quad (1.7)$$

where  $I(t)$  is the invariant. This ensures that the expectation values for the states driven by  $\hat{\mathcal{H}}$  are constant in time. It is possible to expand the state of the system  $|\Psi(t)\rangle$  into the orthonormal basis of the invariant with,

$$|\Psi(t)\rangle = \sum_{n=1}^{\infty} c_n |\psi_n(t)\rangle \quad (1.8)$$

$$|\psi_n(t)\rangle = e^{i\alpha_n(t)} |\phi_n(t)\rangle, \quad (1.9)$$

where  $c_n$  are time-independent amplitudes for each state, and  $|\phi_n(t)\rangle$  are orthonormal

eigenvectors of the invariant, such that

$$I(t) = \sum_n^{\infty} |\phi_n(t)\rangle \lambda_n \langle \phi_n(t)|. \quad (1.10)$$

Here, the  $\lambda_n$  are real constants, and the phase is defined as [12]

$$\alpha_n(t) = \frac{1}{\hbar} \int_0^t \langle \phi_n(t') | i\hbar \frac{\partial}{\partial t'} - \hat{\mathcal{H}}(t') | \phi_n(t') \rangle dt'. \quad (1.11)$$

From here, inverse engineering can be used to create the desired time-dependent Hamiltonian, by imposing some dynamics on the system. The phases,  $\alpha_n(t)$  may be chosen as arbitrary functions to create a time-dependent, unitary evolution operator,

$$U = \sum_n^{\infty} e^{i\alpha_n(t)} |\phi_n(t)\rangle \langle \phi_n(0)|, \quad (1.12)$$

that obeys  $i\hbar \dot{U} = \hat{\mathcal{H}}(t)U$  and the dot is a time-derivative. If one considers Hamiltonians of the Lewis and Leach variety [13],

$$\hat{\mathcal{H}} = \frac{p^2}{2m} - F(t)x + \frac{m}{2}\omega^2(t)x^2 + \frac{1}{\rho(t)^2}U\left[\frac{x-x_c}{\rho(t)}\right] + f(t), \quad (1.13)$$

there will be an invariant that is quadratic in momentum,

$$I = \frac{1}{2m}[\rho(p - m\dot{x}_c) - m\dot{\rho}(x - x_c)]^2 + \frac{1}{2}m\omega_0^2\left(\frac{x - x_c}{\rho}\right)^2 + U\left(\frac{x - x_c}{\rho}\right). \quad (1.14)$$

These equations are valid so long as  $\rho$ ,  $x_c$ ,  $\omega$ , and  $F$  satisfy

$$\ddot{\rho} + \omega^2(t)\rho = \frac{\omega_0^2}{\rho^3} \quad (1.15)$$

$$\ddot{x}_c + \omega^2(t)x_c = F(t)/m, \quad (1.16)$$

with  $\omega_0$  as a constant whose physical interpretation depends on the system. As in the

case of quantum optimal control, additional constraints must be considered to ensure the Hamiltonian and its invariant commute at initial and final times  $t_0$  and  $T$ .

The obvious drawbacks to STA methods are the strengths of quantum optimal control. Where shortcuts can only be used on a specific subset of problems to evolve adiabatically and that are amenable to the analytical methods used, quantum optimal control is a more general tool for a wider variety of systems. On the other hand, STA protocols are semi-analytical and if such protocols can be found, they greatly reduce the computational cost to engineering particular quantum states. Now that I have provided specific examples of methods used in quantum engineering, it is time to put them into practice with an example of creating large-scale superposition states non-adiabatically in the highly-correlated Tonks–Girardeau (TG) gas regime.

### 1.3 Non-adiabatic generation of NOON states in a Tonks–Girardeau gas

For this example application of quantum optimal control and STA protocols, I am interested in generating the maximally entangled  $|N, 0\rangle + |0, N\rangle$  (NOON) state, which is composed of two modes where all particles can be found exclusively in one or the other. Recently, Hallwood *et al.* proposed an experimentally realistic method to generate NOON states in a gas of strongly interacting, neutral bosons on a one-dimensional ring. In this system, different rotational states can be coupled by breaking the rotational symmetry and it is possible to create superposition states with rotating and non-rotating components. Because the atoms are considered to be in the strongly correlated TG gas regime, this process results in a macroscopically-entangled state. It is worth discussing the TG gas in further detail before moving to the precise method of NOON state generation for this example.

### 1.3.1 Tonks–Girardeau gas

As mentioned in Chapter ??, the TG gas consists of a number of bosons that have the properties of spinless, non-interacting fermions. This is a particular case of the one-dimensional Schrödinger equation where the repulsive interaction strength  $g \rightarrow \infty$ . In this case, the bosons cannot be at the same location, which acts formally similar to the Pauli-exclusion principle for fermionic systems. In this case, the bosonic Hamiltonian can be solved by the Bose–Fermi mapping theorem [14, 15], which replaces the interaction terms in the Hamiltonian with a boundary condition on the many-body bosonic wavefunction.

$$\Psi_B(x_1, x_2, \dots, x_N) = 0, \quad \text{if} \quad x_i - x_j = 0 \quad \text{with} \quad i \neq j. \quad (1.17)$$

This allows us then to treat strongly interacting bosons as spinless, non-interacting fermions, for which the many-body wavefunction can be calculated using the Slater determinant [16],

$$\Psi_F(x_1, x_2, \dots, x_N) = \frac{1}{\sqrt{N!}} \det \left[ \psi_n(x_j) \right]_{n,j=1}^N. \quad (1.18)$$

where  $\psi_n(x_j)$  are the single-particle eigenstates of the trapping potential  $V_0$ . Because the fermionic many-body wavefunction is anti-symmetric, it needs to be symmetrized for bosonic states as,

$$\Psi_B(x_1, x_2, \dots, x_N) = \prod_{i < j} \text{sgn}(x_i - x_j) \Psi_F(x_1, x_2, \dots, x_N), \quad (1.19)$$

which means that calculating the time evolution of a TG gas requires evolving single-particle states, governed by a much simpler Hamiltonian.

### 1.3.2 NOON states in a TG gas

Similar to other ring systems introduced in the literature [17, 18], the system suggested by Hallwood *et al.* considers a gas of  $N$  interacting bosons of mass  $m$  on a one-dimensional

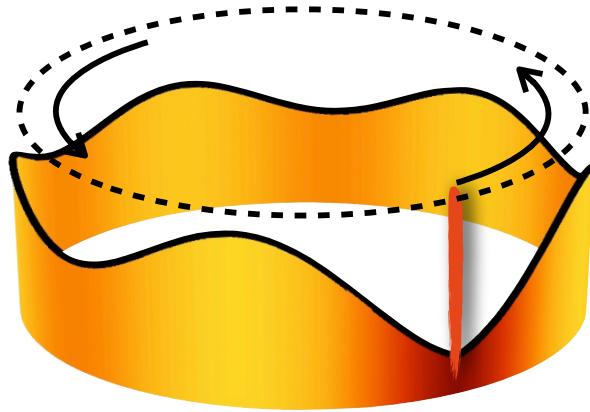


**Figure 1.2:** Schematic of the system. Here, the density profile for five atoms in a TG gas is shown being stirred by a highly localized potential, indicated by the vertical line.

ring with circumference  $L$  [19]. In addition, this system includes a potential barrier, modeled by a Dirac  $\delta$ -function that rotates with an angular frequency  $\Omega$ , as shown in Figure 1.2. In the rotating frame, the scaled Hamiltonian of the system is given by [19]

$$H^{(N)} = \sum_{i=1}^N \left[ \frac{1}{2} \left( -i \frac{\partial}{\partial x_i} - \Omega \right)^2 + b \delta(x_i) + g \sum_{i < j}^N \delta(x_i - x_j) \right], \quad (1.20)$$

where  $b$  is the height of the barrier (in units of  $\hbar^2/mL^2$ ),  $x_i \in [-1/2, 1/2]$  is the position of the  $i$ -th particle (in units of  $L$ ) and  $g$  (in units of  $\hbar^2/mL^2$ ) is the effective interaction strength between the atoms. As discussed in the previous section, the evolution of the full TG gas can be calculated from the evolution of single-particle states, and in the case of this system, the Hamiltonian becomes,

$$H = -\frac{1}{2} \frac{\partial^2}{\partial x^2} + b \delta[x - x_0(t)], \quad (1.21)$$

where  $x_0$  is the position of the barrier at time  $t$ .

The energy spectrum of this system is shown in Figure 1.3 as a function of the rotational frequency  $\Omega \equiv \dot{x}_0/L$  of the system. In Figure 1.3(a) it is shown that in the absence of a barrier, when the eigenstates of  $\hat{\mathcal{H}}$  are plane waves with quantized angular momentum in integer multiples of  $2\pi$ , each angular momentum manifold exists separately such that

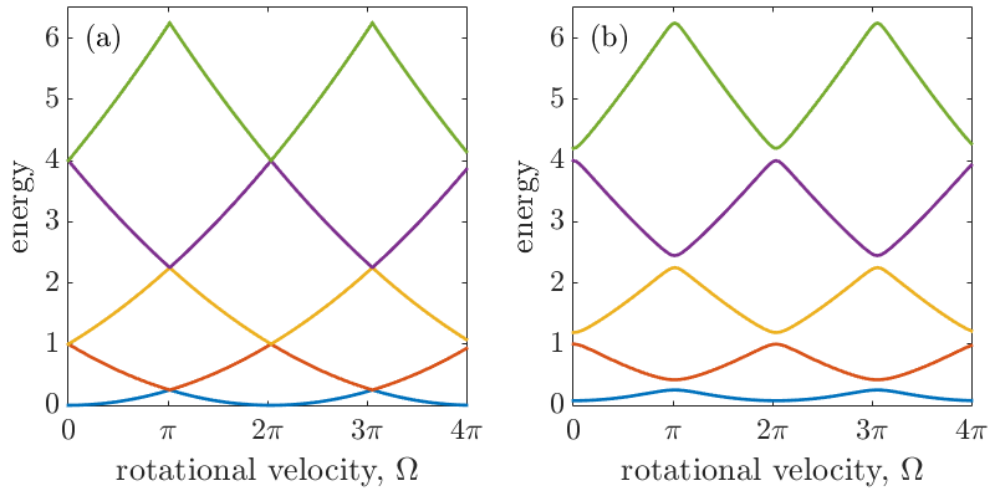


**Figure 1.3:** Single-particle energy spectrum as a function of  $\Omega$  for a barrier height of (a)  $b = 0$  and (b)  $b = 2$ . When a barrier is present in the system, avoided crossings appear in the energy spectrum which grow as the barrier strength increases.

the energy levels cross; however when  $b > 0$  (Figure 1.3(b)), the rotational symmetry is broken and avoided crossings appear in the energy spectrum. This makes transitions between different manifolds possible [20].

By adiabatically accelerating the barrier's rotational frequency from 0 to  $\pi$ , a particle will enter a superposition between two rotational states, and in the case of the TG gas, this will create a macroscopic NOON superposition state between successive values of angular momentum [19]. Any non-adiabatic behavior around the rotational frequencies of the avoided crossing can lead to a transition to a higher energy state and destroy the NOON state. For this reason, the condition for adiabaticity must depend on the gap size, which is dictated by the barrier strength [21]; however, for a delta barrier, the gap size stays constant to first-order approximation [22].

Because this system requires adiabatic movement to properly generate the NOON state, it is difficult to efficiently generate it experimentally. For this reason, it is a perfect example of a system where quantum optimal control and STA protocols can be used to rapidly engineer the appropriate states. For quantum optimal control in this system, a non-adiabatic rotational frequency  $\Omega(t)$  must be found, for which I will use the CRAB

technique with an initial condition of  $\Omega = 0$  and final condition of  $\Omega = \pi$ . For each simulation in the fidelity landscape, this pulse will be modified with procedurally generated sinusoidal functions, calculating the fidelity, and then using the Nelder–Mead method to optimize the result. This will allow one to determine an optimal pulse that maximizes the fidelity of the generated state when compared to the expected NOON state in a pre-set amount of time. For this system, I will show the optimal pulse for the cases where I manipulate the rotational velocity, the barrier height, and both.

For STA protocols, the acceleration process will be split into two, one that breaks the rotational symmetry and another that accelerates the atoms. At the end of the protocol, the potential is lowered to restore rotational symmetry. Here, it is worth mentioning that a FAsT, QUasi-ADiabatic (FAQUAD) shortcut for the creation of superposition states in a TG gas has also been created with some similarities [23].

For both of these methods, instead of calculating the fidelity I calculate the *infidelity*, which is simply  $1 - \mathcal{F} = 1 - |\langle \Psi | \Phi \rangle|^2$ , as the function to minimize. It is also worth mentioning that the fidelity between two many-particle states in a TG gas can be calculated by using the method of mode projections [24, 25],

$$\begin{aligned} \langle \Psi | \Phi \rangle &= \frac{1}{N!} \sum_{\eta, \mu \in P} \epsilon_{\eta} \epsilon_{\mu} \langle \psi_{\eta_1}(x_1) | \phi_{\mu_1}(x_1) \rangle \cdots \langle \psi_{\eta_N}(x_N) | \phi_{\mu_N}(x_N) \rangle \\ &= \det \left[ \langle \psi_i | \phi_j \rangle \right]_{i,j=1}^N \end{aligned} \quad (1.22)$$

which follows directly from the form of the TG state [26]

$$\Psi(x_1, x_2, \dots, x_N) = \frac{1}{\sqrt{N!}} \prod_{i < j} \text{sign}(x_i - x_j) \sum_{\eta \in P} \epsilon_{\eta} \psi_{\eta_1}(x_1) \cdots \psi_{\eta_N}(x_N). \quad (1.23)$$

Here  $P$  represents the set of all permutations of  $N$  elements,  $\epsilon_{\eta}$  represents the anti-symmetric tensor of the permutation  $\eta$ , and  $\psi_i$  represent the orbitals. Now I will discuss the findings with both optimal control and STA protocols.

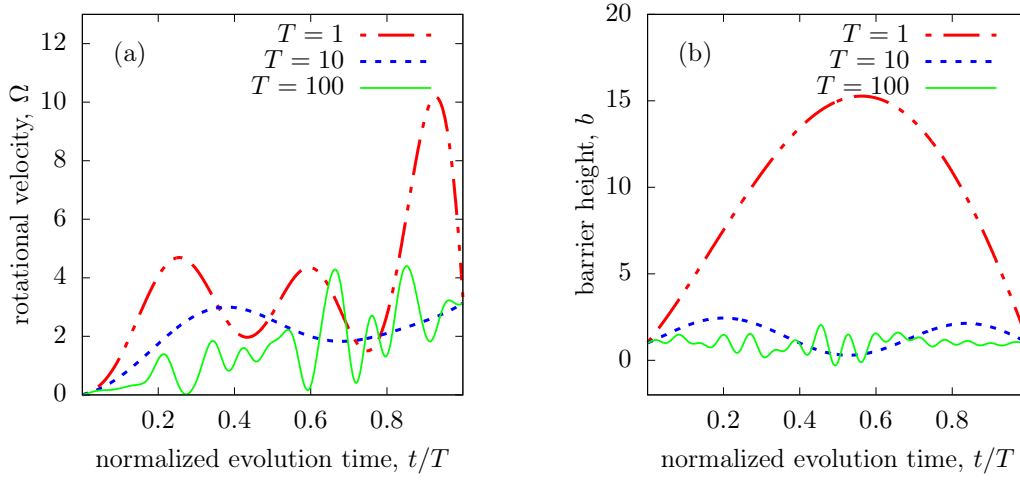


**Figure 1.4:** Accelerating a single particle from the ground state with  $J = 15$ . (a) Optimal rotational velocity pulses for  $T = 1, 10$ , and  $100$  for fixed barrier height  $b = 1$ . (b) Optimal barrier height for a linearly increasing rotational velocity,  $\Omega = \pi t/T$  for  $T = 1, 10$ , and  $100$ .

### 1.3.3 Optimal control protocols

First, I will focus on the acceleration of a single particle, initially in the ground state of the system. Figure 1.4 (a) shows the results of this simulation if the barrier height is kept constant and one assumes an initial unmodified pulse that corresponds to a linear ramp from  $\Omega = 0$  to  $\pi$  for a preset total time,  $T$ . For longer evolution times, there are many local maxima for the fidelity, and as such, longer evolution times effectively produce noisy signals and the Nelder–Mead method converges on one of many local minima. For shorter evolution times, the pulse greatly affects the system and the shapes vary greatly from the initial linear ramp. The infidelities for the linear guess pulse and its corresponding optimized pulse can be found in Figure 1.6, and one can see an improvement of several orders of magnitude. Here, for longer evolution times, the initial linear pulse is a reasonable method to generate NOON states with an infidelity of  $10^{-2}$  because it is already close to adiabatic; however, even in this case, the NOON state generation fidelity is better with optimization. For all optimal control results in this Chapter, the CRAB method was run



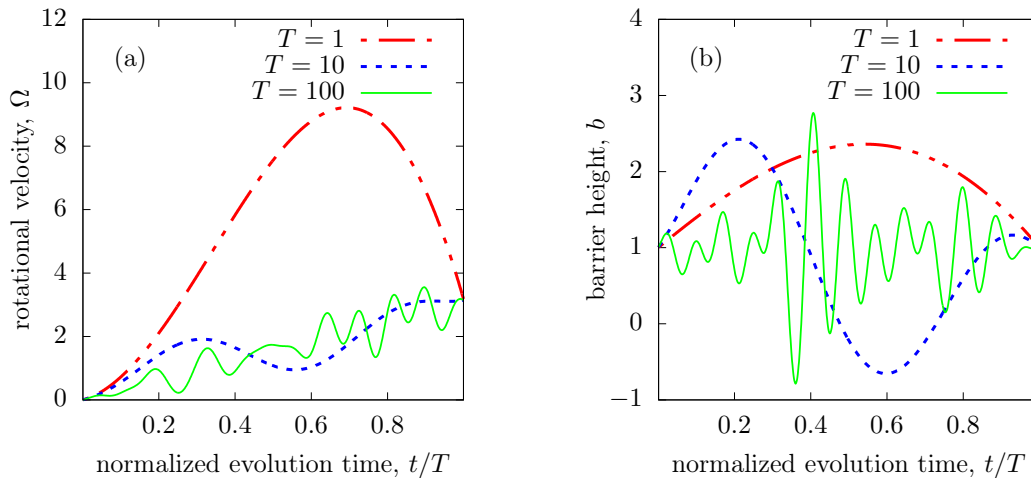


**Figure 1.5:** Optimal pulses to accelerate a single particle initially in the ground state of the trap for  $T = 1, 10$ , and  $100$  for the (a) rotational velocity and (b) barrier height when optimizing over both simultaneously.

100 times and the data with the highest fidelity was kept.

For optimizations of the barrier strength, a simple linear ramp for  $\Omega$  and an initial and final height for the barrier of  $b = 1$  were chosen. The optimal pulses for the barrier height for  $T = 1, 10$ , and  $100$  are shown in Figure 1.4(b) and shorter evolution times similarly produce larger deviations from the initial pulse. Again these pulses lead to significant improvements in the fidelity shown in Figure 1.6.

With the CRAB method, it is possible to optimize over as many control parameters as one would like, and as such, it is possible to optimize over both the barrier strength and rotational frequency. The results can be seen in Figure 1.5, where (a) is the modified rotational frequency and (b) is the barrier height. When comparing to the previous cases, similar trends emerge. In particular, shorter evolution times result in less noisy optimizations when compared to longer evolution. Even so, all sets of pulses are radically different when compared to optimizations over a single variable. When comparing the fidelities in Figure 1.6, it is clear that optimizations over rotation alone provide the simplest method to optimize the fidelity. It is likely that each run of the CRAB method is stuck in a

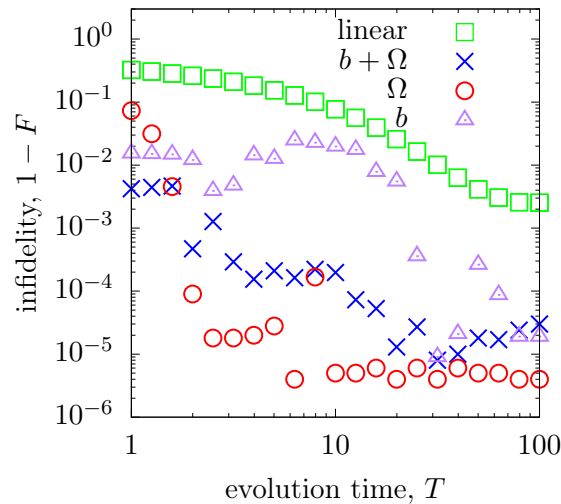


**Figure 1.6:** Infidelities as a function of the overall process time for optimally controlled rotational acceleration, barrier height, or both. Here, 'linear' refers to an unoptimized linear acceleration from  $\Omega = 0$  to  $\pi$  while keeping the barrier height fixed at  $b = 1$ .

local minimum in the fidelity landscape at some point and that optimization over both variables can provide the same optimization as rotating, alone.

As such, when discussing the dynamics of a TG gas with 3 and 5 particles, I have only optimized over rotation. Because of the Bose–Fermi mapping theorem, the evolution of an  $N$ -particle TG gas can be calculated by evolving a gas of  $N$  spinless fermions. In the zero-temperature limit, the fermions in the initial and target state create a Fermi sea by filling the lowest  $N$  energy levels. In this case, only atoms near the Fermi edge can transition into empty states and it is thus crucial to optimize the dynamics of the overall gas with respect to the particle with highest energy [23]. In Figure 1.7, I show the fidelity for the particle closest to the Fermi edge and the entire TG gas for  $N = 3$  and 5. In this figure, one can see that by performing the optimization for the atoms near the Fermi edge, one can increase the fidelity of the entire gas for certain regimes; however, in contrast to Figure 1.6, there seems to be no fidelity increase from a linear pulse for short evolution times. One can also see a crossover regime where optimizations of the particle at the Fermi edge seem to fail, but evolution of the entire gas is still slightly better than the

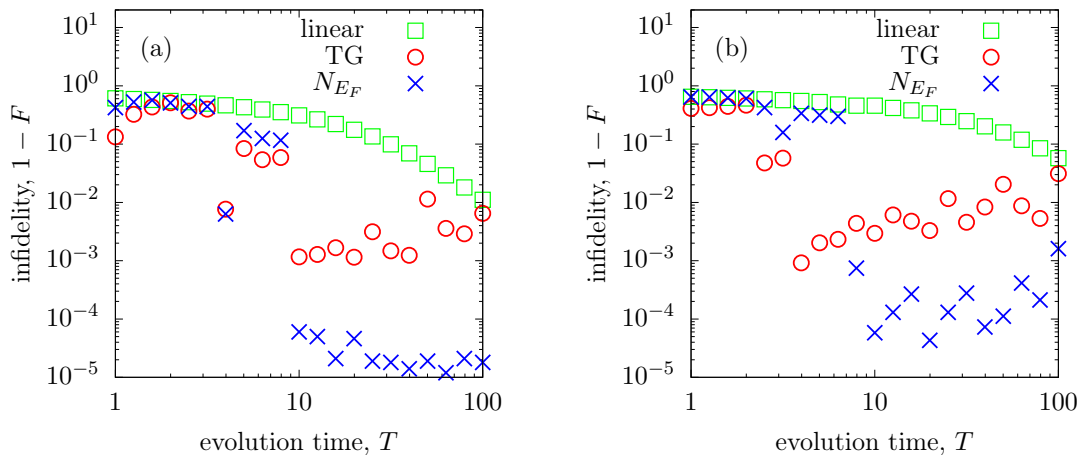


**Figure 1.7:** Infidelities for the evolution of a TG gas with (a)  $N = 3$  and (b)  $N = 5$  particles using the CRAB optimal control technique. The optimal pulses were determined for the particle at the Fermi edge (blue crosses), and applied to the whole gas (red circles). Here, the green squares show the fidelity of a linear pulse for the atom closest to the Fermi edge. A clear range where the CRAB algorithm is effective for generating NOON states with multiple particles can be clearly identified.

linear pulse. It is clear that the CRAB method creates highly effective pulses; however, for very short and long evolution times, the fidelity increase from a linear pulse is not as drastic.

### 1.3.4 Results with STA protocols

In this section, I will describe an STA protocol to generate NOON states in this system non-adiabatically, and though this was mentioned briefly in Section 1.3.2, it will be described more rigorously here. In this case, we start out with rotational symmetry and break break this symmetry by introducing a time-dependent external potential at  $t = 0$  and removing in the end. For this, we do not choose a  $\delta$  function, but instead a harmonic or sinusoidal potential along the ring.

The protocol consists of five steps:

1. Adiabatic raising of a weak harmonic or sinusoidal potential around the ring.

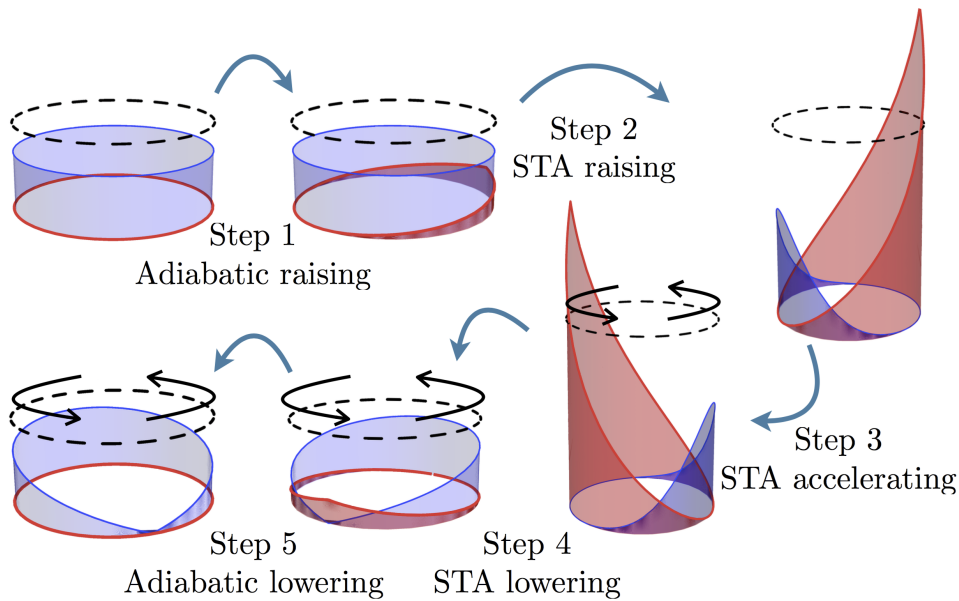


**Figure 1.8:** Scheme for the acceleration of a single atom using STA. In this example, the homogeneous ground state gets localized, accelerated and released at the angular velocity of  $\Omega = \pi$  into the state  $(\exp(i2\pi x) + 1) / \sqrt{2}$ . The atomic density is indicated in blue and the potential is in red.

2. Fast tightening of this potential to localize the particles.
3. Accelerating the particles by moving the center of the potential.
4. Loosening the potential by reversing step 2.
5. Adiabatic lowering of the harmonic or sinusoidal potential.

A schematic of this process is shown in Figure 1.8. For steps 2-4, pre-existing STA protocols can be used, and these will be discussed in this section. The full protocol for the TG ring example will follow the STA methods outlined above with Lewis–Riesenfeld invariants and in this case, one needs to fulfill boundary conditions such that  $\hat{\mathcal{H}}(t_0) = \hat{\mathcal{H}}(T) = p^2/2m$ . To be clear, the NOON states created with the STA protocol are slightly different those generated with quantum optimal control, as the STA variant does not rely on a  $\delta$  barrier.

One of the two shortcuts explored for this system involves raising and lowering a harmonic potential [27, 28]. For this shortcut, a stationary harmonic potential is required

and  $F$ ,  $x_c$ , and  $U$  from Equation (1.13) can all be set to zero, leading to

$$\hat{\mathcal{H}} = -\frac{1}{2} \frac{\partial^2}{\partial x^2} + \frac{1}{2} \omega^2(t) x^2. \quad (1.24)$$

To change the frequency while keeping the commutation relations and  $\omega(t)$  continuous, one must impose the following conditions:

$$\begin{aligned} \rho(t_0) &= 1, & \rho(t_f) &= \gamma = \sqrt{\omega_0/\omega_f}, \\ \dot{\rho}(t_0) &= 0, & \dot{\rho}(t_f) &= 0, \\ \ddot{\rho}(t_0) &= 0, & \ddot{\rho}(t_f) &= 0. \end{aligned} \quad (1.25)$$

Which, together with Equations (1.15) and (1.25) allow one to choose any form of  $\rho$ . A good choice is the polynomial,

$$\rho(s) = 6(\gamma - 1)s^5 - 15(\gamma - 1)s^4 + 10(\gamma - 1)s^3 + 1, \quad (1.26)$$

where  $s = (t - t_0)/(t_f - t_0)$  allows one to numerically find a solution for  $\omega(t)$  that leads to the squeezing or expansion of the particle wavefunction with high fidelity in a short time. As an important note, for small values of  $\omega_0$ , Equation (1.15) leads to purely imaginary values for  $\omega(t)$ , corresponding to repulsive potentials. In order to avoid this and because the final states of this protocol require the external potential to be absent, the first and final steps in the protocol for this system involves adiabatically raising and lowering a potential to a suitable  $\omega_0$  value.

Once the potential has been raised, it is time to accelerate the particles to the chosen frequency, and a shortcut for this process with a harmonic trap exists [29–31]. In the rotational shortcut, the trapping frequency is held constant and the position of the potential is modified. This means that  $U = 0$ ,  $F = \omega_0^2 x_0(t)$ , and

$$H = -\frac{1}{2} \frac{\partial^2}{\partial x^2} + \frac{1}{2} \omega_0^2 (x - x_0(t))^2. \quad (1.27)$$

Here, Equation (1.16) becomes the only relevant auxiliary equation,

$$\ddot{x}_c + \omega_0^2(x_c - x_0) = 0, \quad (1.28)$$

and the conditions that must be imposed on  $x_c$ , are such that

$$\begin{aligned} x_c(t_0) &= x_0(t_0), & x_c(t_f) &= d, \\ \dot{x}_c(t_0) &= 0, & \dot{x}_c(t_f) &= \Omega_f, \\ \ddot{x}_c(t_0) &= 0, & \ddot{x}_c(t_f) &= 0, \end{aligned} \quad (1.29)$$

where  $d$  is the final position of the potential minimum and  $\Omega_f$  is its final velocity. For most applications of this shortcut,  $d$  is important, and  $\Omega_f$  is set to zero; however, this case is the opposite.

Like for the shortcut for raising the potential, the exact form of  $x_c$  can be chosen somewhat arbitrarily, and a convenient choice is

$$x_c(s) = (6d - 3\Omega_f)s^5 - (15d - 7\Omega_f)s^4 + (10d - 4\Omega_f)s^3 + x_0(t_0), \quad (1.30)$$

where, as above,  $s$  is the normalized time. The value of  $\Omega_f$  can then be chosen to be odd multiples of  $\pi$  to generate the desired NOON states.

Unlike the shortcut to raise the potential, this shortcut is only approximate and works best when  $\omega$  is large so that the particles are highly localized. Both of these shortcuts rely on the presence of a harmonic potential of the form

$$V_H(x, t) = \frac{1}{2}\omega^2(t)(x - x_0(t))^2, \quad (1.31)$$

where  $\omega$  is the frequency of the trap (in units of  $\hbar/mL^2$ ) and  $x_0$  the position of its minimum. In the case of the TG ring, the potential must be symmetric around  $x_0$ , such that it is continuous at  $x = \pm 1/2$ ; therefore, the real form of  $(x - x_0)$  must be  $(x - x_0 + 1/2)(\text{mod } 1) - 1/2$ . The potential  $V_H$  is then continuous everywhere on the ring, but its

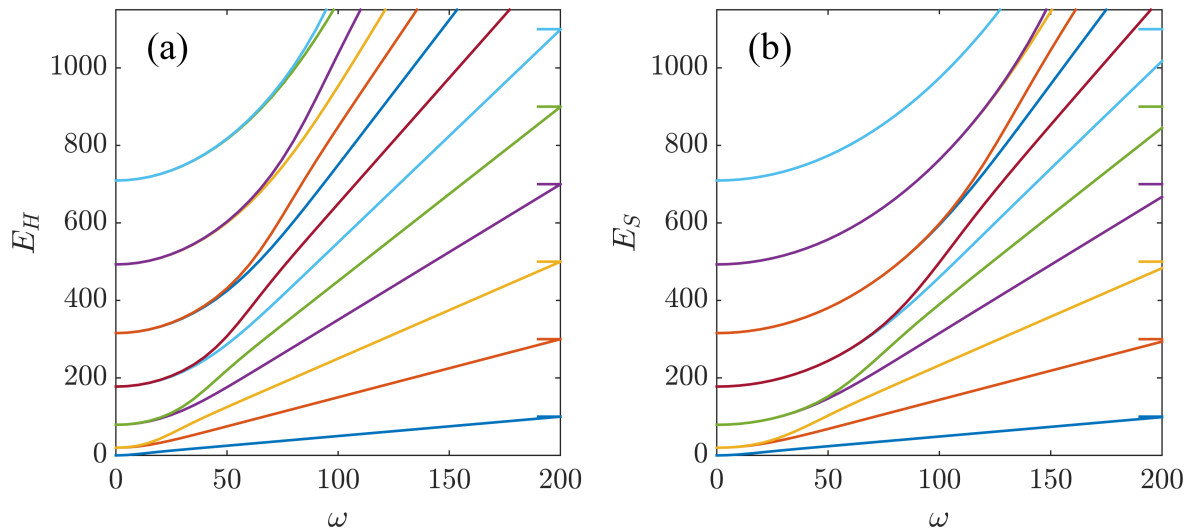


**Figure 1.9:** Energy eigenspectrum of the system with (a) a harmonic or (b) a sinusoidal potential as a function of  $\omega$ . The eigenstates continuously change from angular momentum states of energy  $E_k = 2\pi^2 k^2$  (with  $k = 0, \pm 1, \dots$ ) at  $\omega = 0$ , towards harmonic-oscillator states of energy  $E_n = \omega(n + 1/2)$  (with  $n = 0, 1, \dots$ ) for large  $\omega$ . For comparison, the horizontal lines on the right vertical axis give the energy levels in a harmonic potential with  $\omega = 200$ .

derivative is discontinuous at  $x = x_0 + 1/2$  because this position is diametrically opposite to  $x_0$ . Though  $V_H$  is easy to work with theoretically, it is not necessarily experimentally realistic, and for this reason, we also consider a sinusoidal potential of the form [32, 33],

$$V_S(x, t) = \frac{\omega^2(t)}{2\pi^2} \sin^2(\pi(x - x_0(t))), \quad (1.32)$$

where the notation is the same as before. Here, prefactors are chosen such that  $V_H$  is an approximation of  $V_S$  around  $x_0$ .

In Figure 1.9 I show the difference between the two potentials by computing the energy spectra of both Hamiltonians. Here, the eigenstates at  $\omega = 0$  are the angular momentum states  $e^{i2\pi kx}$ , with degenerate clockwise and counterclockwise momentum states of opposite quantum number  $k$ . As  $\omega$  is increased, the degeneracy ceases and the spectrum asymptotically approaches that of a harmonic oscillator. For the sinusoidal case, the difference with the harmonic spectrum increases with the quantum number  $n$ .

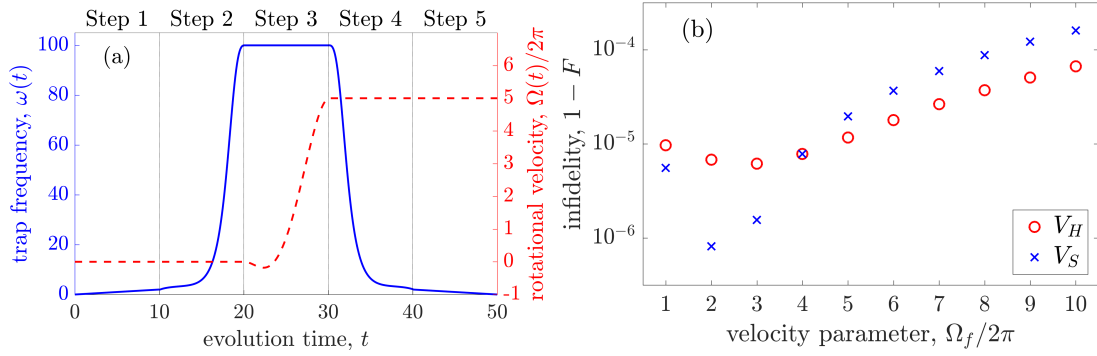


**Figure 1.10:** (a) Plot of the parameters  $\omega(t)$  and the angular velocity  $\Omega(t)$  for the entire protocol. The parameters are  $\omega_0 = 2$ ,  $\omega_f = 100$ ,  $d = 100$ , each step is executed in  $t_f - t_0 = 10$ , and  $\Omega_f$  is picked depending on the desired output state (here,  $\Omega_f = 5 \times 2\pi$ ). (b) Final infidelities for  $\Omega_f = 1, 2, \dots, 10 \times 2\pi$  for  $V_H$  (dotted blue line) and  $V_S$  (solid red line). The rest of parameters are as shown in (a).

Like the case of quantum optimal control, I will first show the single-particle results. In Figure 1.10(a), the values for  $\omega(t)$  and  $\Omega(t)$  are shown, and in Figure 1.10(b), the infidelities for the state preparation of plane waves  $e^{i\Omega_f x}$  with  $\Omega_f = 1 \dots 10 \times 2\pi$  are shown. Here, it is clear that even for a large amount of angular momentum, the fidelities remain high for both the harmonic and sinusoidal potentials.

For a multi-particle case in the TG regime, the initial states for the particles will be eigenstates of free space, which are simply plane waves  $e^{i2\pi kx}$  with integer  $k$ . Because the states with  $\pm k$  are degenerate, it is equally valid to consider the initial eigenstates

$$\phi_0^i(x) = 1, \quad (1.33)$$

$$\phi_{2l-1}^i(x) = \frac{1}{\sqrt{2}} (e^{i2\pi lx} - e^{-i2\pi lx}) = i\sqrt{2} \sin(2l\pi x), \quad (1.34)$$

$$\phi_{2l}^i(x) = \frac{1}{\sqrt{2}} (e^{i2\pi lx} + e^{-i2\pi lx}) = \sqrt{2} \cos(2l\pi x), \quad (1.35)$$

for  $l = \{1, 2, \dots\}$ . These states have a total angular momentum of zero and are well-suited for the provided STA protocol because when an odd number of particles occupies the lower eigenstates, the sin/cos pairs are guaranteed to be populated.

For  $\Omega_f = \pi$ , the plane wave of quantum numbers  $k + 1$  and  $-k$  are degenerate and



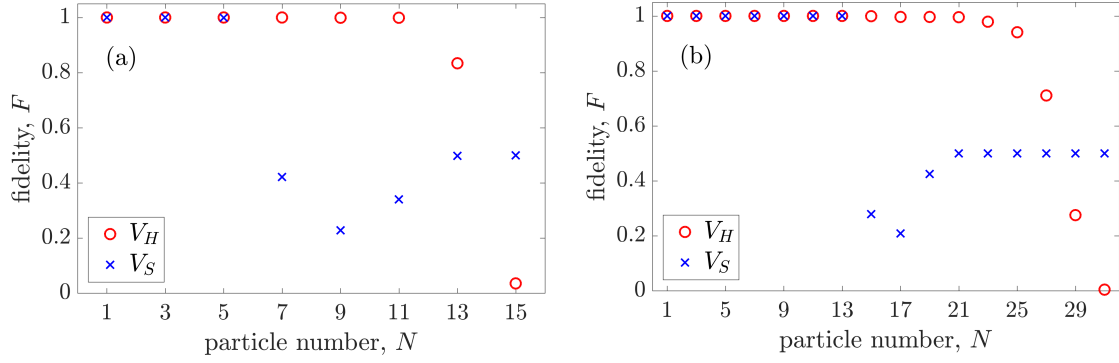


**Figure 1.11:** Final fidelities  $F$  of TG states of increasing particle number for the protocol shown in Figure 1.10(a) with  $\Omega_f = \pi$  for  $V_H$  (red circle) and  $V_S$  (blue cross). Plot (a) shows the fidelity of the protocol with  $\omega_f = 100$  and (b) with  $\omega_f = 200$ .

one can construct the target states

$$\phi_{2l}^t(x) = \frac{1}{\sqrt{2}} (e^{i2\pi(l+1)x} + e^{-i2\pi lx}) = \sqrt{2} \cos[(2l+1)\pi x] e^{i\pi x}, \quad (1.36)$$

$$\phi_{2l+1}^t(x) = \frac{1}{\sqrt{2}} (e^{i2\pi(l+1)x} - e^{-i2\pi lx}) = i\sqrt{2} \sin[(2l+1)\pi x] e^{i\pi x}, \quad (1.37)$$

for  $l = 0, 1, 2, \dots$ . The states with total angular momentum  $\pi$  are similar to NOON states.

Any initial state  $|\phi_l^i\rangle$  can be brought to the target state  $|\phi_l^t\rangle$  with high fidelity with the proposed protocol, and the process also works for TG gases. In Figure 1.11(a), the harmonic potential fidelities are shown to remain high for  $N \leq 11$  after which they decrease due to a finite maximum height of the potential enforced by periodic boundary conditions. The fidelities can be improved by increasing the maximum trapping frequency  $\omega_f$  as was demonstrated in Figure 1.11(b) where the value of  $\omega_f$  is doubled and the fidelities remain high until  $N \leq 21$ . When using the sinusoidal potential, the fidelity drops for smaller particle numbers compared to the harmonic potential (although it also increases with  $\omega_f$ ), due to the lower height  $V_S$  has compared to  $V_H$ .

## 1.4 Outlook

In this chapter, quantum optimal control and STA protocols were introduced to optimize quantum engineering tasks in cold atomic gases. I have introduced a physical system to generate NOON states in a TG gas non-adiabatically with both methods, and they were shown to be highly effective. Such dynamical evolution techniques require time-dependent control parameters, such as rotation frequency or barrier height, and allowing for these dynamic operations has hitherto been a difficult task on GPU hardware. In the following chapter, I will discuss GPU hardware in-depth and also tackle this issue, along with several others noted in Chapter ??.

# Bibliography

- [1] J. Werschnik and E. K. U. Gross. Quantum optimal control theory. *Journal of Physics B: Atomic, Molecular and Optical Physics*, 40(18):R175, 2007.
- [2] D. Guéry-Odelin, A. Ruschhaupt, A. Kiely, E. Torrontegui, S. Martínez-Garaot, and J. G. Muga. Shortcuts to adiabaticity: concepts, methods, and applications. *arXiv preprint arXiv:1904.08448*, 2019.
- [3] J. Schloss, A. Benseny, J. Gillet, J. Swain, and Th. Busch. Non-adiabatic generation of NOON states in a Tonks–Girardeau gas. *New Journal of Physics*, 18(3):035012, 2016.
- [4] F. L. Lewis, D. Vrabie, and V. L. Syrmos. *Optimal control*. John Wiley & Sons, 2012.
- [5] S. Ruder. An overview of gradient descent optimization algorithms. *arXiv preprint arXiv:1609.04747*, 2016.
- [6] J. A. Nelder and R. Mead. A Simplex Method for Function Minimization. *The Computer Journal*, 7(4):308–313, 01 1965. ISSN 0010-4620. doi: 10.1093/comjnl/7.4.308. URL <https://doi.org/10.1093/comjnl/7.4.308>.
- [7] J. R. Koza. Genetic programming. 1997.
- [8] T. G. Kolda, R. M. Lewis, and V. Torczon. Optimization by direct search: New perspectives on some classical and modern methods. *SIAM review*, 45(3):385–482, 2003.

- 
- [9] R. M. Lewis, A. Shepherd, and V. Torczon. Implementing generating set search methods for linearly constrained minimization. *SIAM Journal on Scientific Computing*, 29(6):2507–2530, 2007.
- [10] H. Pohlheim. Examples of objective functions. *Retrieved*, 4(10):2012, 2007.
- [11] E. Torrontegui, S. Ibáñez, S. Martínez-Garaot, M. Modugno, A. del Campo, D. Guéry-Odelin, A. Ruschhaupt, X. Chen, and J. G. Muga. Shortcuts to adiabaticity. In *Advances in atomic, molecular, and optical physics*, volume 62, pages 117–169. Elsevier, 2013.
- [12] H. R. Lewis Jr and W. B. Riesenfeld. An exact quantum theory of the time-dependent harmonic oscillator and of a charged particle in a time-dependent electromagnetic field. *Journal of Mathematical Physics*, 10(8):1458–1473, 1969.
- [13] H. R. Lewis and P. G. L. Leach. A direct approach to finding exact invariants for one-dimensional time-dependent classical hamiltonians. *Journal of Mathematical Physics*, 23(12):2371–2374, 1982.
- [14] M. D. Girardeau, E. M. Wright, and J. M. Triscari. Ground-state properties of a one-dimensional system of hard-core bosons in a harmonic trap. *Phys. Rev. A*, 63:033601, Feb 2001. doi: 10.1103/PhysRevA.63.033601. URL <https://link.aps.org/doi/10.1103/PhysRevA.63.033601>.
- [15] M. D. Girardeau and E. M. Wright. Measurement of one-particle correlations and momentum distributions for trapped 1d gases. *Phys. Rev. Lett.*, 87:050403, Jul 2001. doi: 10.1103/PhysRevLett.87.050403. URL <https://link.aps.org/doi/10.1103/PhysRevLett.87.050403>.
- [16] J. C. Slater. The theory of complex spectra. *Physical Review*, 34(10):1293, 1929.
- [17] K. K. Das, M. D. Girardeau, and E. M. Wright. Interference of a thermal Tonks gas on

- a ring. *Phys. Rev. Lett.*, 89:170404, Oct 2002. doi: 10.1103/PhysRevLett.89.170404. URL <https://link.aps.org/doi/10.1103/PhysRevLett.89.170404>.
- [18] M. D. Girardeau and A. Minguzzi. Motion of an impurity particle in an ultra-cold quasi-one-dimensional gas of hard-core bosons. *Phys. Rev. A*, 79:033610, Mar 2009. doi: 10.1103/PhysRevA.79.033610. URL <https://link.aps.org/doi/10.1103/PhysRevA.79.033610>.
- [19] D. W. Hallwood, T. Ernst, and J. Brand. Robust mesoscopic superposition of strongly correlated ultracold atoms. *Phys. Rev. A*, 82:063623, Dec 2010. doi: 10.1103/PhysRevA.82.063623. URL <http://link.aps.org/doi/10.1103/PhysRevA.82.063623>.
- [20] C. Schenke, A. Minguzzi, and F. W. J. Hekking. Probing superfluidity of a mesoscopic Tonks–Girardeau gas. *Physical Review A*, 85(5):053627, 2012.
- [21] A. Nunnenkamp, A. M. Rey, and K. Burnett. Generation of macroscopic superposition states in ring superlattices. *Phys. Rev. A*, 77:023622, Feb 2008. doi: 10.1103/PhysRevA.77.023622. URL <https://link.aps.org/doi/10.1103/PhysRevA.77.023622>.
- [22] D. W. Hallwood, K. Burnett, and J. Dunningham. The barriers to producing multiparticle superposition states in rotating Bose–Einstein condensates. *Journal of Modern Optics*, 54(13-15):2129–2148, 2007.
- [23] S. Martínez-Garaot, A. Ruschhaupt, J. Gillet, Th. Busch, and J. G. Muga. Fast quasiadiabatic dynamics. *Phys. Rev. A*, 92:043406, Oct 2015. doi: 10.1103/PhysRevA.92.043406. URL <https://link.aps.org/doi/10.1103/PhysRevA.92.043406>.
- [24] A. del Campo. Long-time behavior of many-particle quantum decay. *Phys. Rev. A*,

- 84:012113, Jul 2011. doi: 10.1103/PhysRevA.84.012113. URL <https://link.aps.org/doi/10.1103/PhysRevA.84.012113>.
- [25] K. Lelas, T. Ševa, and H. Buljan. Loschmidt echo in one-dimensional interacting Bose gases. *Phys. Rev. A*, 84:063601, Dec 2011. doi: 10.1103/PhysRevA.84.063601. URL <https://link.aps.org/doi/10.1103/PhysRevA.84.063601>.
- [26] M. Girardeau. Relationship between systems of impenetrable bosons and fermions in one dimension. *Journal of Mathematical Physics*, 1(6):516–523, 1960.
- [27] Xi Chen and J. G. Muga. Transient energy excitation in shortcuts to adiabaticity for the time-dependent harmonic oscillator. *Phys. Rev. A*, 82:053403, Nov 2010. doi: 10.1103/PhysRevA.82.053403. URL <https://link.aps.org/doi/10.1103/PhysRevA.82.053403>.
- [28] X. Chen, A. Ruschhaupt, S. Schmidt, A. del Campo, D. Guéry-Odelin, and J. G. Muga. Fast optimal frictionless atom cooling in harmonic traps: Shortcut to adiabaticity. *Phys. Rev. Lett.*, 104:063002, Feb 2010. doi: 10.1103/PhysRevLett.104.063002. URL <https://link.aps.org/doi/10.1103/PhysRevLett.104.063002>.
- [29] S. Masuda and K. Nakamura. Fast-forward of adiabatic dynamics in quantum mechanics. *Proceedings of the Royal Society A: Mathematical, Physical and Engineering Sciences*, 466(2116):1135–1154, 2009.
- [30] E. Torrontegui, S. Ibáñez, Xi Chen, A. Ruschhaupt, D. Guéry-Odelin, and J. G. Muga. Fast atomic transport without vibrational heating. *Phys. Rev. A*, 83:013415, Jan 2011. doi: 10.1103/PhysRevA.83.013415. URL <https://link.aps.org/doi/10.1103/PhysRevA.83.013415>.
- [31] S. Masuda. Acceleration of adiabatic transport of interacting particles and rapid manipulations of a dilute Bose gas in the ground state. *Phys. Rev. A*, 86:063624,

- Dec 2012. doi: 10.1103/PhysRevA.86.063624. URL <https://link.aps.org/doi/10.1103/PhysRevA.86.063624>.
- [32] C.F. Phelan, T. Hennessy, and Th. Busch. Shaping the evanescent field of optical nanofibers for cold atom trapping. *Opt. Express*, 21(22):27093–27101, Nov 2013. doi: 10.1364/OE.21.027093. URL <http://www.opticsexpress.org/abstract.cfm?URI=oe-21-22-27093>.
- [33] S. Masuda, K. Nakamura, and A. del Campo. High-fidelity rapid ground-state loading of an ultracold gas into an optical lattice. *Phys. Rev. Lett.*, 113:063003, Aug 2014. doi: 10.1103/PhysRevLett.113.063003. URL <https://link.aps.org/doi/10.1103/PhysRevLett.113.063003>.